25716980

Periodontal Defects in the A116T Knock-in Murine Model of Odontohypophosphatasia

B.L. Foster[1]*, C.R. Sheen[2]*, N.E. Hatch[3], J. Liu[3], E. Cory[4], S. Narisawa[2], T. Kiffer-Moreira[2], R.L. Sah[4], M.P. Whyte[5,6], M.J. Somerman[1], and J.L. Millán[2]

Abstract

Mutations in *ALPL* result in hypophosphatasia (HPP), a disease causing defective skeletal mineralization. *ALPL* encodes tissue nonspecific alkaline phosphatase (ALP), an enzyme that promotes mineralization by reducing inorganic pyrophosphate, a mineralization inhibitor. In addition to skeletal defects, HPP causes dental defects, and a mild clinical form of HPP, odontohypophosphatasia, features only a dental phenotype. The *Alpl* knockout (*Alpl*$^{-/-}$) mouse phenocopies severe infantile HPP, including profound skeletal and dental defects. However, the severity of disease in *Alpl*$^{-/-}$ mice prevents analysis at advanced ages, including studies to target rescue of dental tissues. We aimed to generate a knock-in mouse model of odontohypophosphatasia with a primarily dental phenotype, based on a mutation (c.346G>A) identified in a human kindred with autosomal dominant odontohypophosphatasia. Biochemical, skeletal, and dental analyses were performed on the resulting *Alpl*$^{+/A116T}$ mice to validate this model. *Alpl*$^{+/A116T}$ mice featured 50% reduction in plasma ALP activity compared with wild-type controls. No differences in litter size, survival, or body weight were observed in *Alpl*$^{+/A116T}$ versus wild-type mice. The postcranial skeleton of *Alpl*$^{+/A116T}$ mice was normal by radiography, with no differences in femur length, cortical/trabecular structure or mineral density, or mechanical properties. Parietal bone trabecular compartment was mildly altered. *Alpl*$^{+/A116T}$ mice featured alterations in the alveolar bone, including radiolucencies and resorptive lesions, osteoid accumulation on the alveolar bone crest, and significant differences in several bone properties measured by micro–computed tomography. Nonsignificant changes in acellular cementum did not appear to affect periodontal attachment or function, although circulating ALP activity was correlated significantly with incisor cementum thickness. The *Alpl*$^{+/A116T}$ mouse is the first model of odontohypophosphatasia, providing insights on dentoalveolar development and function under reduced ALP, bringing attention to direct effects of HPP on alveolar bone, and offering a new model for testing potential dental-targeted therapies in future studies.

Keywords: alkaline phosphatase, hypophosphatasia, bone, cementum, dentin, periodontium

Introduction

Loss-of-function mutations in *ALPL* result in hypophosphatasia (HPP), an inborn error of metabolism that features defective mineralization of the skeleton and dentition (Whyte 2012). *ALPL* encodes tissue nonspecific alkaline phosphatase (TNAP; alternately, TNSALP), an enzyme that reduces local concentrations of the mineralization inhibitor, inorganic pyrophosphate (Millán 2013). Skeletal complications of HPP include rickets and osteomalacia, with clinical severity ranging widely from profound skeletal hypomineralization that is lethal at birth to dental defects alone. Dental manifestations include cementum deficiency, tooth loss, thin dentin, widened pulp chambers, malformed roots, and enamel alterations (Foster, Nociti, et al. 2014; Foster, Ramnitz, et al. 2014). Dental hard tissues seem exceptionally sensitive to HPP, as the clinical form odontohypophosphatasia affects only the dentition (Reibel et al. 2009).

The *Alpl* knockout (*Alpl*$^{-/-}$) mouse recapitulates the metabolic and skeletal phenotype of severe infantile HPP (Narisawa et al. 1997; Fedde et al. 1999). We demonstrated in *Alpl*$^{-/-}$ mice

[1]National Institute of Arthritis and Musculoskeletal and Skin Diseases, National Institutes of Health, Bethesda, MD, USA
[2]Sanford Children's Health Research Center, Sanford-Burnham Medical Research Institute, La Jolla, CA, USA
[3]Department of Orthodontics and Pediatric Dentistry, School of Dentistry, University of Michigan, Ann Arbor, MI, USA
[4]Department of Bioengineering, University of California, San Diego, La Jolla, CA, USA
[5]Center for Metabolic Bone Disease and Molecular Research, Shriners Hospital for Children, St. Louis, MO, USA
[6]Division of Bone and Mineral Diseases, Washington University School of Medicine, St. Louis, MO, USA
*Authors contributing equally to this article.

Corresponding Author:
J.L. Millán, Sanford Children's Health Research Center, Sanford-Burnham Medical Research Institute, La Jolla, CA, USA.
Email: millan@sanfordburnham.org

defects in cementum, dentin, alveolar bone, and enamel (McKee et al. 2011; Foster et al. 2012; Yadav et al. 2012; Foster, Nagatomo, et al. 2013; Zweifler et al. 2015). However, these mice die by 2 to 3 wk of age, preventing analysis of milder forms of HPP at advanced ages, including studies to rescue dental tissues.

We aimed to create a knock-in mouse model of odontohypophosphatasia. The *Alpl* c.346G>A mutation, predicting an A116T substitution, was selected for knock-in based on homology with the predominantly dental phenotype of a large well-characterized HPP kindred (Hu et al. 2000) and dominant-negative effect in vitro of the causal mutation (Lia-Baldini et al. 2001; Fauvert et al. 2009; Ishida et al. 2011). We hypothesized that a mouse heterozygous for the A116T mutation ($Alpl^{+/A116T}$) would phenocopy odontohypophosphatasia and serve as a model for further studies of HPP dental disease.

Materials and Methods

Knock-in Vector Design and Synthesis

Mouse experiments were approved by the Institutional Animal Care and Use Committee of the Sanford Burnham Medical Research Institute (La Jolla, CA, USA). Methods for vector design and in vitro expression analysis are detailed in the Appendix. The targeting construct to introduce the c.346G>A base change into exon 5 of *Alpl* is shown in Figure 1A. Sequencing confirmed germline transmission (Fig. 1B). The $Alpl^{A116T}$ mouse line was maintained by breeding wild-type (WT) mice with heterozygote mice ($Alpl^{+/A116T}$). $Alpl^{+/A116T}$ and WT mice were analyzed at 27 d postnatal (dpn) and 4 and 14 mo.

Plasma Chemistry Analysis

Blood was collected by cardiac puncture, transferred into lithium-heparinized tubes (Becton, Dickinson & Co., Franklin Lakes, NJ, USA), and plasma was separated by centrifugation at $3,000 \times g$ for 10 min. Alkaline phosphatase (ALP) activity, phosphorus, and calcium were measured using a VetScan Comprehensive Diagnostic Profile rotor (Abaxis, Union City, CA, USA).

Radiography

Radiographs of skeletons were obtained with an MX-20 Specimen Radiographic System (Faxitron X-ray Corp., Chicago, IL, USA) and inspected by 2 blinded independent analysts familiar with HPP skeletal disease. Femoral length was measured using MicroDicom software (Sofia, Bulgaria). Hemimandibles were scanned in a cabinet X-ray (Faxitron X-ray Corp.) at 30 kV for 40 s.

Micro–computed Tomography

Methods for micro–computed tomography (micro-CT) analysis are detailed in the Appendix. Femora were scanned on a Skyscan 1076 micro-CT scanner (Kontich, Belgium), and

regions of interest were determined using established guidelines (Bouxsein et al. 2010). Skulls were scanned on an eXplore Locus SP micro-CT scanner (GE Healthcare, London, ON, Canada), and regions of interest for the parietal and frontal bones were determined as described previously (Liu et al. 2013) and measured using established algorithms (Meganck et al. 2009; Umoh et al. 2009). For dentoalveolar analysis, dissected mandibles were scanned on a Scanco Medical μCT 35 (Scanco Medical AG, Brüttisellen, Switzerland). DICM files were reoriented using ImageJ software (1.48r), with coronal, sagittal, and transverse planes of section chosen for comparison.

Parameters analyzed by microCT included total cross-sectional tissue area (Tt.Ar), cortical bone area (Ct.Ar), cortical area fraction (Ct.Ar/Tt.Ar), cortical thickness (Ct.Th), tissue mineral density (TMD), tissue volume (TV), bone surface (BS), bone volume (BV), trabecular thickness (Tb.Th), trabecular spacing (Tb.Sp), trabecular number (Tb.N), structure model index (SMI), and bone mineral density (BMD), bone mineral content (BMC), and tissue mineral content (TMC) (Bouxsein et al. 2010).

Three-point Bone Bending

Three-point bone bending was performed to determine the mechanical properties of the femur, using an Instron 3342 material testing machine (Instron, Norwood, MA, USA) fitted with a 100-N load cell. The span was fixed at 10 mm, and the cross-head was lowered at 1 mm/min. Load (N) and extension (mm) were recorded every 0.2 s until fracture. Maximum stiffness, work to fracture, and failure and fracture points were calculated from load-extension curves as described previously (Aspden 2003).

Histology

Mandibles used for histology were decalcified in AFS (10% v/v glacial acetic acid, 4% v/v neutral buffered formalin, and 0.85% w/v sodium chloride in water) by stirring at 4 °C for 3 to 4 wk, then processed in paraffin to make serial 6-μm sections. To evaluate periodontal ligament collagen fiber organization, sections were stained by the picrosirius red method with 0.2% phosphomolybdic acid hydrate, 0.4% Direct Red 80, and 1.3% 2,4,6-trinitrophenol (Polysciences, Inc., Warrington, PA, USA), as described previously (Foster 2012). Staining for tartrate-resistant acid phosphatase to identify osteoclasts was performed following the manufacturer's instructions (Wako Chemicals, Japan). Briefly, deparaffinized sections were incubated at 37 °C for 60 min with staining solution containing sodium tartrate, followed by counterstaining with nuclear stain, air-drying, and mounting.

Immunohistochemistry was performed on histologic sections using an avidin-biotinylated peroxidase-based kit (Vectastain Elite, Vector Labs, Burlingame, CA) with a 3-amino-9-ethylcarbazole substrate (Vector Labs) to produce a red product. Primary antibodies included rat monoclonal anti-human ALPL (R&D Systems, Minneapolis, MN, USA;
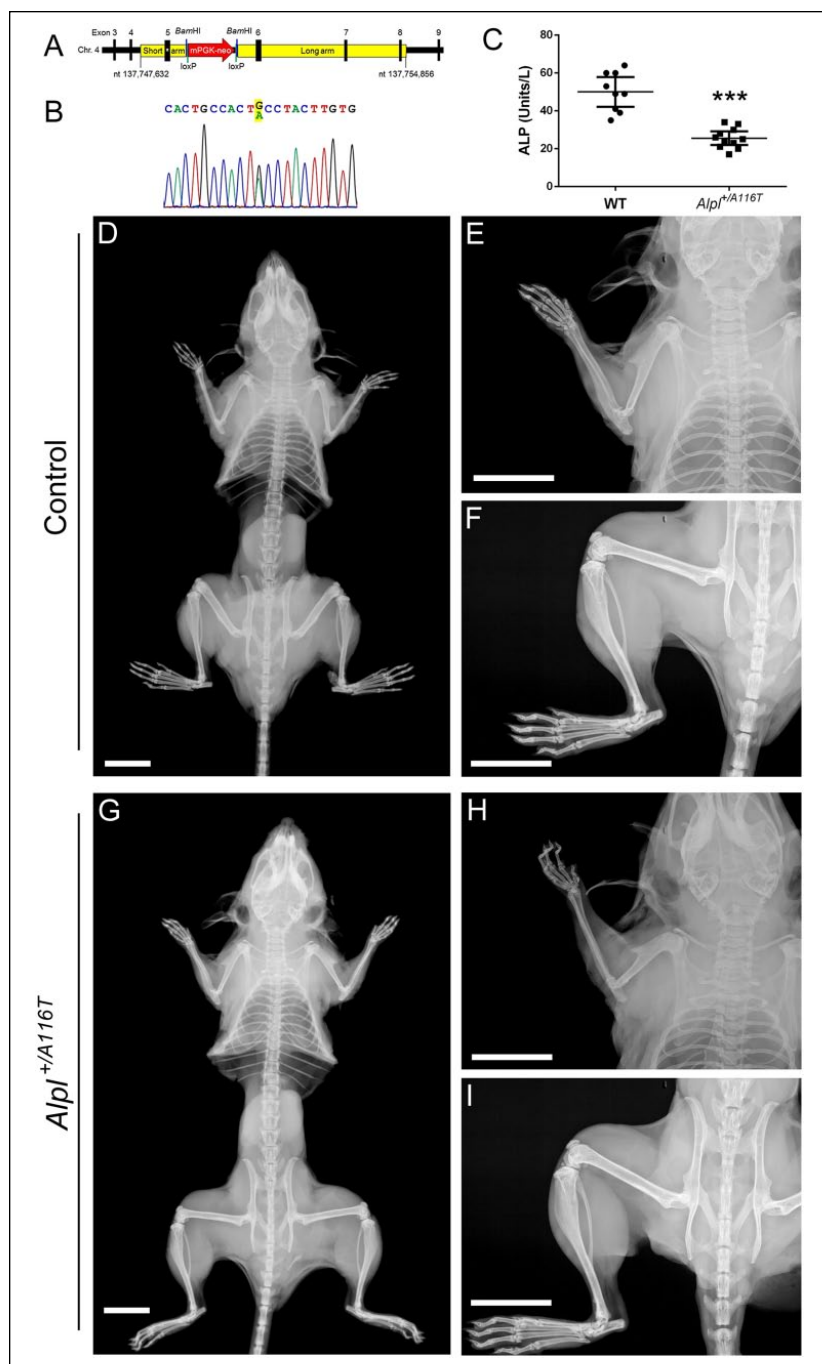
Figure 1. Postcranial bone phenotype is not altered by the *Alpl* A116T mutation in mice. (**A**) Schematic representation of the targeting construct used to introduce the c.346G>A (A116T) mutation into the *Alpl* locus. The construct consists of short and long arms (yellow) separated by a neomycin gene under the control of the mouse phosphoglycerol kinase promoter (red), flanked by loxP recognition sites (green lines), inserted into a *Bam*HI restriction site (blue lines) in intron 5 of *Alpl*. The nucleotide positions (nt) of the ends of the construct on chromosome 4 are given. (**B**) Electropherogram of DNA extracted from knock-in mice showing successful knock-in of the c.346G>A (highlighted) mutation into the *Alpl* locus. (**C**) Plasma collected from wild-type (WT; *n* = 7) and *Alpl*[+/A116T] (*n* = 9) mice at 120 d postnatal showed a 50% decrease in mean alkaline phosphatase (ALP) activity in *Alpl*[+/A116T] mice (***P* < 0.001 by 2-tailed Student's *t* test). Values are reported on the scatter plot as individual measurements (mean ± 95% confidence interval). (**D–I**) Radiography of WT and *Alpl*[+/A116T] heterozygous male mice at 120 d postnatal showing whole animals (D, G), left forelimbs (E, H), and left hind limbs (F, I). No overt skeletal pathology was detected in *Alpl*[+/A116T] mice at this age. Scale bar indicates 10 mm for all panels (C–H).

Zweifler et al. 2015), rabbit polyclonal anti-mouse bone sialoprotein (Dr. Renny Franceschi, University of Michigan, Ann Arbor, MI, USA; Foster, Soenjaya, et al. 2013), rabbit polyclonal LF-175 anti-mouse osteopontin (Dr. Larry Fisher, National Institute of Dental and Craniofacial Research, Bethesda, MD, USA; Foster 2012), goat polyclonal anti-mouse receptor activator of nuclear factor kappa-B ligand (RANKL; R&D Systems), and rabbit polyclonal anti-human periostin (POSTN; Abcam Inc., Cambridge, MA, USA).

Samples used for undecalcified sectioning were fixed in paraformaldehyde, embedded in methylmethacrylate, and von Kossa stained as described previously (Foster, Soenjaya, et al. 2013).

Histomorphometry

Acellular cementum width was measured on lingual and buccal surfaces of the first mandibular molar mesial root 100 μm from the cementoenamel junction and on lingual surfaces of incisors. Mean values for WT (*n* = 5 to 6) and *Alpl*[+/A116T] (*n* = 7 to 9) cementum thickness were compared by the independent-samples *t* test. Serum ALP levels were correlated to incisor and molar acellular cementum thickness using Pearson's *r* coefficient. Cellular cementum area was measured using ImageJ software. Alveolar bone height was quantitated as distance from cementoenamel junction to the alveolar bone crest on the lingual and buccal aspects. Statistical analyses were performed using GraphPad Prism 6.01 (La Jolla, CA, USA).

Results

Alpl A116T Mutation in Mice Reduces Their Plasma ALP Activity

No significant differences in litter size, survival to weaning, or survival to 120 dpn were observed between WT and *Alpl*[+/A116T] male mice (data not shown). Body weight did not differ significantly between genotypes (*P* > 0.05), averaging 31.6 ± 1.4 g for WT and 30.4 ± 0.6 g for *Alpl*[+/A116T] male mice at 120 dpn.

Plasma biochemistry analysis indicated no differences between genotypes in calcium and phosphorus concentrations (Appendix Table 2). However, ALP activity was significantly reduced in *Alpl*[+/A116T]

versus WT mice (Fig. 1C, Appendix Table 2). Mean ALP was reduced by 50% in $Alpl^{+/A116T}$ mice (25.6 ± 5.4 vs. 50 ± 10.2 U/L in WT), with ALP of individual heterozygotes ranging from 34% to 68% of the WT mean. This range in plasma ALP in $Alpl^{+/A116T}$ mice reflects a similarly broad range reported in the human kindred (Hu et al. 2000). Notably, ALP in $Alpl^{+/A116T}$ mice was higher than the activity observed in vitro in cotransfected cells (with WT and mutant alleles), which produced only 32.5% of WT activity (Appendix Table 3).

Postcranial Skeletal Phenotype Is Not Altered in Alpl$^{+/A116T}$ Mice

By radiography, no differences were observed between postcranial skeletons (i.e., the skeleton lying posterior to the skull) of WT and $Alpl^{+/A116T}$ mice at 120 dpn, including no evidence of malformations, fractures, rickets, calcific periarthritis, chondrocalcinosis, or pseudogout (Fig. 1D–I). Femur length did not differ ($P > 0.05$) between groups (17.1 ± 0.1 for both WT and $Alpl^{+/A116T}$). Similarly, radiographic analysis at age 14 mo did not reveal any skeletal abnormalities (data not shown). Micro-CT analysis of femora indicated no differences in cortical or trabecular bone structure or density (Appendix Table 4). Three-point bending analysis indicated no differences in failure or fracture loads, work to fracture, or stiffness between WT and $Alpl^{+/A116T}$ femurs (Appendix Table 5).

Alterations in Cranial Bones in Alpl$^{+/A116T}$ Mice

Frontal bones of $Alpl^{+/A116T}$ mice were not different from WT mice (Appendix Table 6). Parietal bone mineral content, bone mineral density, tissue mineral content, and BV/TV were not different from controls. However, BS/BV and trabecular number were increased, while Tb.Th was decreased ($P < 0.05$ for all) in $Alpl^{+/A116T}$ compared to WT mice.

Alpl$^{+/A116T}$ Mice Feature Alveolar Bone Defects

$Alpl^{-/-}$ mice manifest mineralization defects in alveolar bone, dentin, cementum, and enamel (Millán et al. 2008; McKee et al. 2011; Foster et al. 2012; Yadav et al. 2012; Foster,
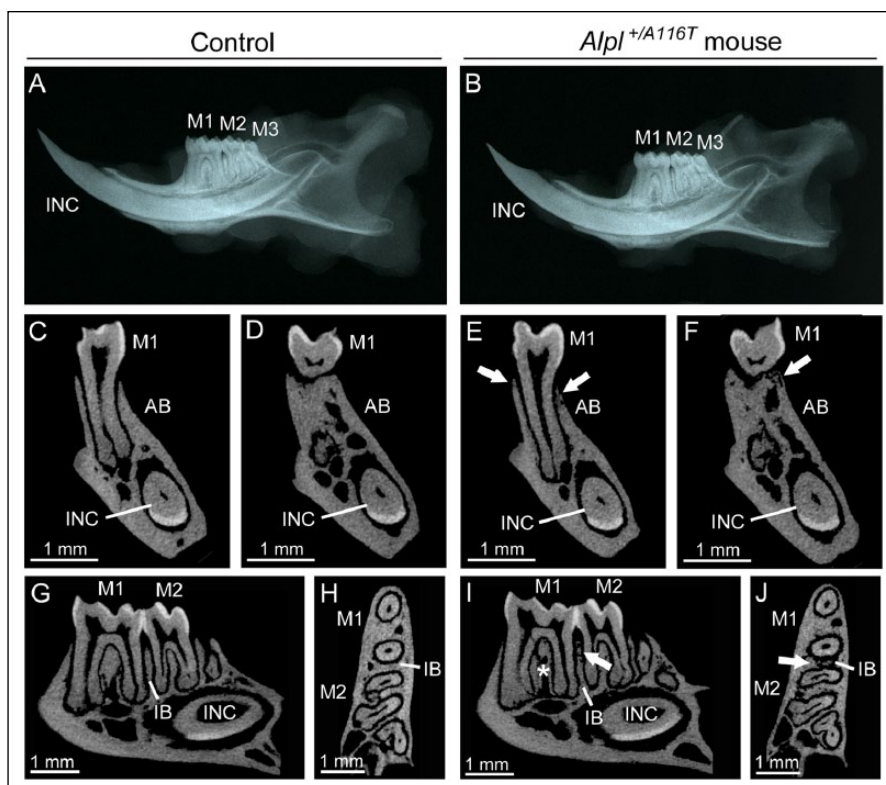

Figure 2. $Alpl^{+/A116T}$ mice feature alveolar bone (AB) defects. (**A**, **B**) Radiography reveals no overt differences in wild-type control versus $Alpl^{+/A116T}$ mandibles, molars (M1 to M3), or incisors (INC) at 120 d postnatal. (**C**, **E**) Micro–computed tomography (micro-CT) cut sections in the coronal plane at the first molar mesial root indicate radiolucency (white arrows in E) at the alveolar bone crest in $Alpl^{+/A116T}$ versus wild-type controls. (**D**, **F**) Micro-CT coronal plane sections at the first molar root furcation region reveal lesions consistent with osteoclastic resorption (white arrows in F) in the alveolar bone of $Alpl^{+/A116T}$ mice. (**G**, **I**) Micro-CT sagittal plane sections show alterations in alveolar bone in the furcation region (white asterisk in I) and resorptive type lesions in interproximal bone (IB) between first and second molars of $Alpl^{+/A116T}$ mice (white arrow in I). (**H**, **J**) Micro-CT transverse plane sections located 500 μm apical to the cementoenamel junction show extensive loss of interproximal bone between first and second molar roots (white arrow in J).

Nagatomo, et al. 2013). The Appendix Figure is included for reference to dental defects in $Alpl^{-/-}$ mice.

No gross differences in $Alpl^{+/A116T}$ versus WT mandibles were indicated by radiography at 120 dpn (Fig. 2A, B). Micro-CT revealed radiolucency in alveolar bone surrounding the first molars of $Alpl^{+/A116T}$ mice, while molars and incisors appeared unaltered (Fig. 2C vs. E). $Alpl^{+/A116T}$ mouse alveolar bone featured regions consistent with resorptive lesions in lingual and interproximal bone surrounding first and second molars (Fig. 2D vs. F, G vs. I, H vs. J).

Quantitative micro-CT analysis was performed on 2 regions of alveolar bone associated with first molars (Table). In the furcation region, $Alpl^{+/A116T}$ mice featured significantly reduced alveolar bone tissue mineral density ($P < 0.01$) indicating bone hypomineralization and decreased Tb.Th ($P < 0.05$) and increased BS/BV ($P < 0.05$) indicating alterations in trabecular bone (similar to patterns noted for parietal bone in Appendix Table 6) compared with WT. In lingual alveolar bone, $Alpl^{+/A116T}$ mice featured significantly reduced TV ($P < 0.05$), BV ($P < 0.01$), and BV/TV ($P < 0.05$), reflecting reduced bone in this region. Micro-CT analysis of dental tissues revealed reduced

Table. Micro–computed Tomography Analysis of Alveolar Bone.

Parameter	Furcation		Lingual Aspect	
	WT	*Alpl*[+/A116T]	WT	*Alpl*[+/A116T]
TV, mm^3	0.31 ± 0.03	0.30 ± 0.02	0.13 ± 0.01	0.12 ± 0.01[a]
BV, mm^3	0.20 ± 0.02	0.19 ± 0.01	0.11 ± 0.01	0.09 ± 0.02[b]
BV/TV, %	64.78 ± 5.56	62.57 ± 2.90	82.09 ± 3.50	73.65 ± 8.81[a]
TMD, g HA/cm^3	1.07 ± 0.02	1.04 ± 0.01[b]	0.98 ± 0.02	0.96 ± 0.02
Tb.N, 1/mm	6.68 ± 0.53	7.16 ± 0.92	N/A	N/A
Tb.Th, mm	0.15 ± 0.02	0.13 ± 0.01[a]	N/A	N/A
Tb.Sp, mm	0.19 ± 0.02	0.17 ± 0.03	N/A	N/A
BS/BV, mm^2/mm^3	19.55 ± 1.87	21.55 ± 1.07[a]	N/A	N/A

Alveolar bone associated with first mandibular molars was compared at 120 d postnatal in wild-type (WT; *n* = 7) and *Alpl*[+/A116T] mice (*n* = 9). Values are reported as means ± SD.
BS, bone surface; BV, bone volume; Tb.N, trabecular number; Tb.Sp, trabecular spacing; Tb.Th, trabecular thickness; TMD, tissue mineral density; TV, tissue volume.
[a]$P < 0.05$. Independent-samples *t* test.
[b]$P < 0.01$. Independent-samples *t* test.

BV/TV for *Alpl*[+/A116T] mouse molar enamel and root dentin but no other differences (Appendix Table 7).

Delays in *Alpl*[+/A116T] mouse alveolar bone mineralization were indicated by accumulation of osteoid (approximately 10 to 30 μm thick) on alveolar bone crests (Fig. 3A–D), consistent with osteomalacia in the radiolucent regions observed by micro-CT. Previously, we reported increased osteopontin expression as a causative factor in mineralization defects in *Alpl*^{-/-} mice (Harmey et al. 2004; Harmey et al. 2006; McKee et al. 2011; Foster, Nagatomo, et al. 2013). In *Alpl*[+/A116T] mice, however, osteopontin deposition appeared unaltered in teeth and surrounding bone (Fig. 3E–H). TNAP distribution by immunohistochemistry also appeared normal in the periodontium of *Alpl*[+/A116T] mice versus controls (Fig. 3I vs. K). Because alterations in mineralization of tooth or bone, including HPP, can lead to defective periodontal attachment, picrosirius red staining was performed to evaluate collagen fiber organization. PDL fibers were observed to be well organized, with no insertion defects identified at the tooth or bone surfaces of *Alpl*[+/A116T] mice (Fig. 3J vs. L).

Areas of apparent bone resorption were also determined on histologic sections. *Alpl*[+/A116T] mice at 120 dpn featured localized alveolar bone resorption associated with numerous tartrate-resistant acid phosphatase–positive osteoclast-like cells (Fig. 3M, O). RANKL was identified by immunohistochemistry in some cells bordering areas of resorption, but the levels were not remarkable in *Alpl*[+/A116T] versus WT tissues (data not shown). Areas of extensive resorption featured a mix of connective tissue with fibroblasts, blood vessels, and marrow space, indicated by periostin immunostaining (Fig. 3N, P). Alveolar bone resorption was not observed in *Alpl*[+/A116T] mice by micro-CT or histology at 27 dpn (data not shown).

In light of an apparent increase in resorption in *Alpl*[+/A116T] alveolar bone, histomorphometry was performed to search for changes in alveolar bone height. No differences were identified in alveolar bone height in *Alpl*[+/A116T] compared to WT (data not shown; $P = 0.74$ and 0.78 for lingual and buccal aspects, respectively).

Acellular Cementum Thickness Is Correlated with Serum ALP

HPP causes absent or reduced acellular cementum formation (as in the *Alpl*^{-/-} mouse; Appendix Fig.; Foster, Nociti, et al. 2014). We confirmed presence of both acellular and cellular cementum by histology (Fig. 4A–H) and immunohistochemistry (e.g., Fig. 3F, H). However, acellular cementum appeared thin in *Alpl*[+/A116T] mouse molars and incisors, and histomorphometry suggested a nonsignificant trend toward decreased thickness compared to WT mice ($P = 0.09$ for incisor cementum; $P = 0.07$ and 0.14 for molar lingual and buccal acellular cementum, respectively; Fig. 4I). Cellular cementum featured hypomineralized regions (cementoid), confirmed by von Kossa staining at 27 dpn (Fig. 4G inset vs. 4E inset). Cellular cementum area was not altered in *Alpl*[+/A116T] versus controls ($P = 0.46$ and 0.40 for buccal and lingual sides, respectively; Fig. 4J). Plasma levels of circulating residual ALP activity were correlated positively with incisor acellular cementum thickness in WT and *Alpl*[+/A116T] mice ($P = 0.03$), with nonsignificant "trends" ($P = 0.05$ and 0.09) in molar acellular cementum thickness (Fig. 4K, L).

Discussion

To define the long-term effects of relatively mild HPP on the mineralized dentoalveolar tissues, we generated the first knock-in mouse model of HPP. Our model featured a c.346G>A point mutation in exon 5 of *Alpl*, resulting in an A116T amino acid substitution. *Alpl*[+/A116T] mice featured a mean 50% reduction in plasma ALP, with individual values ranging from 34% to 68% of WT. Postcranial skeletal elements were unaffected in *Alpl*[+/A116T] mice, and parietal bones in the skull were mildly affected in diploe (trabecular) measurements. The A116T mutation caused hypomineralization of mouse alveolar bone and cellular cementum, with a trend of reduced acellular cementum. Acellular cementum of molars and incisors was correlated with plasma ALP activity.
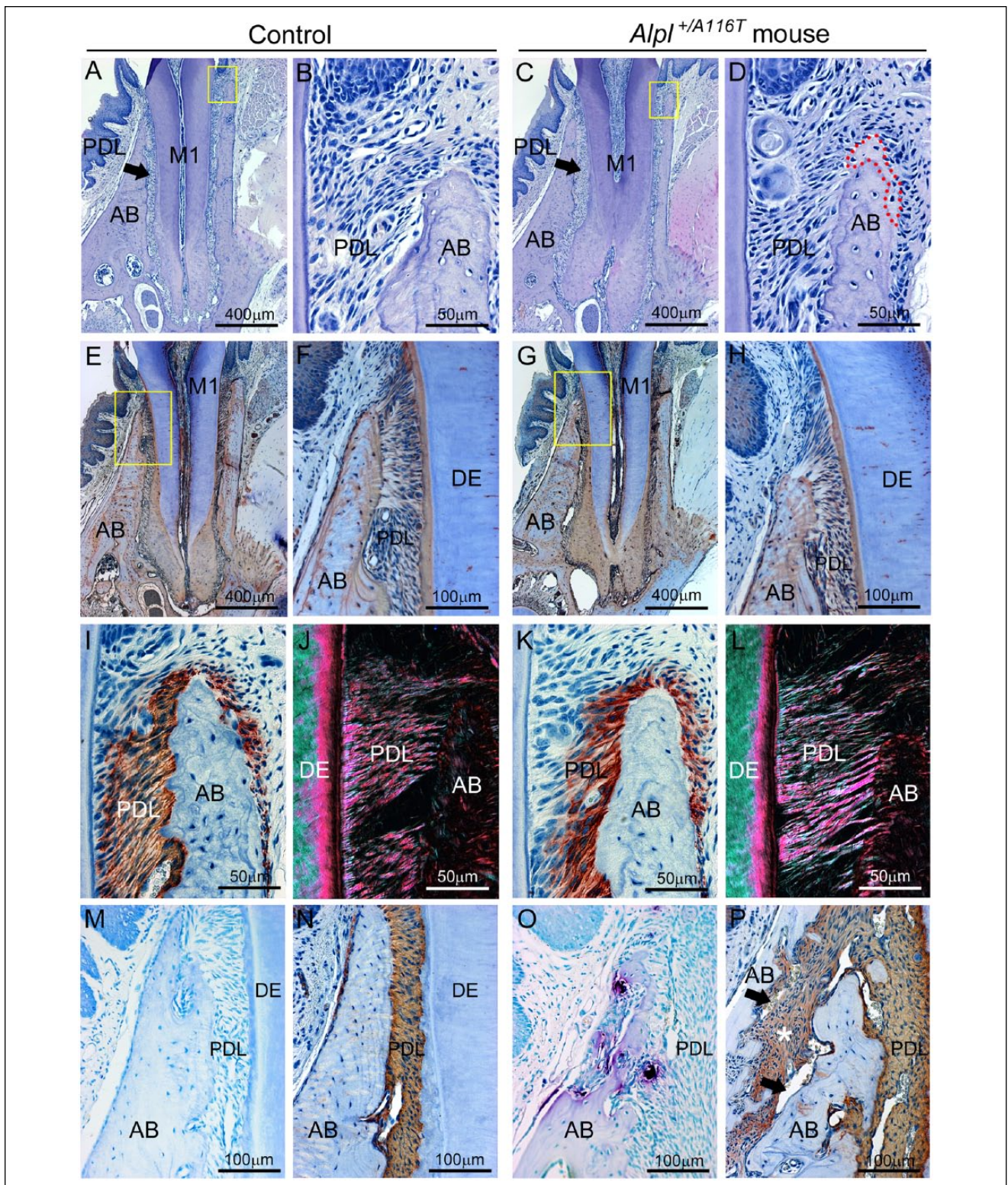
Figure 3. Delayed mineralization and increased resorption in alveolar bone of *Alpl*[+/A116T] mice. (**A–D**) Histologic sections of mandibular dentoalveolar tissues from 120 d postnatal mice feature overtly normal first molars (M1), while *Alpl*[+/A116T] mice feature accumulation of osteoid (area outlined in dotted red line in D) at the alveolar bone (AB) crest. Yellow boxes in A and C represent regions shown in B and D, respectively. (**E–H**) Immunohistochemistry (IHC) reveals no differences in osteopontin localization in tooth or bone of *Alpl*[+/A116T] mice versus wild-type controls. Yellow boxes in E and G represent regions shown in F and H, respectively. No differences in *Alpl*[+/A116T] versus wild type are noted for (**I, K**) tissue nonspecific alkaline phosphatase intensity or localization by IHC, or (**J, L**) collagen organization of the periodontal ligament (PDL), as shown by picrosirius red staining under polarized light microscopy. (**M, O**) Regions of bone resorption in *Alpl*[+/A116T] mice are associated with numerous TRAP-positive osteoclast-like (purple-red, multinucleated) cells on the bone surface. (**N, P**) IHC for periostin indicates that regions of extensive alveolar bone resorption in *Alpl*[+/A116T] tissues feature a mix of connective tissue (white star) and blood vessels (black arrows). DE, dentin.
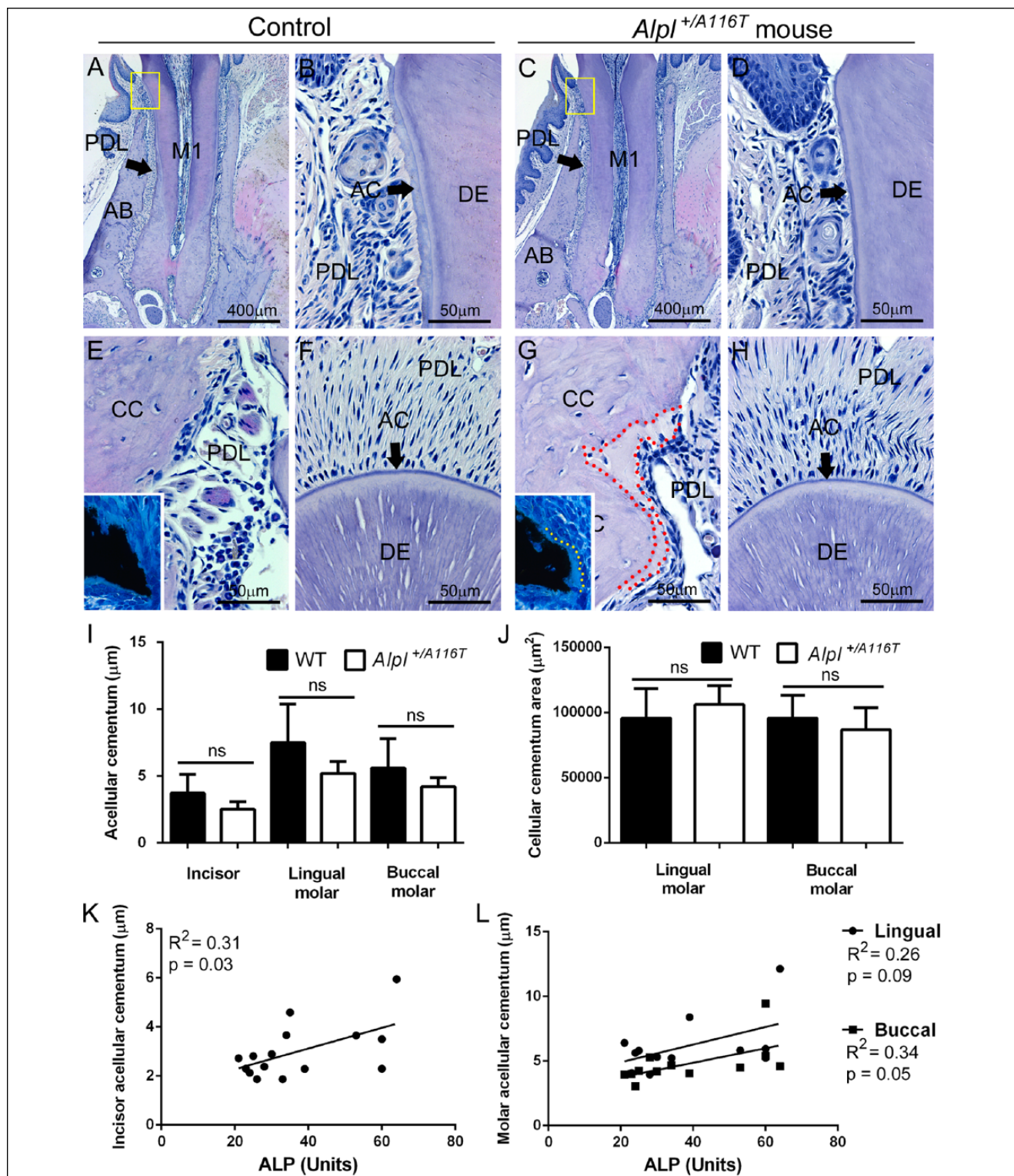
Figure 4. Acellular cementum thickness is correlated with serum alkaline phosphatase (ALP). (**A–D**) Histologic sections of mandibular first molar teeth (M1) from 120 d postnatal *Alpl*[+/A116T] mice suggest thin acellular cementum (AC; arrows where notated) compared with controls. Yellow boxes in A and C represent regions shown in B and D, respectively. (**E, G**) Compared with well-mineralized wild-type (WT) cellular cementum (CC), *Alpl*[+/A116T] mice feature an accumulated cementoid layer (area outlined in dotted red line in G). Insets in E and G show von Kossa staining, where *Alpl*[+/A116T] mouse molars feature a thick layer of unmineralized cementoid not observed in WT mice. (**F, H**) The acellular cementum of the *Alpl*[+/A116T] mandibular incisor appears thin compared with WT. (**I**) Histomorphometry of acellular cementum width in first molars (bucal and lingual aspects) and incisors reveals no statistically significant differences in *Alpl*[+/A116T] versus WT mice ($P > 0.05$; not significant [ns]). (**J**) Histomorphometry of cellular cementum area in first molars (buccal and lingual aspects) reveals no differences in *Alpl*[+/A116T] versus WT mice. (**K**) Serum ALP is significantly positively correlated with incisor acellular cementum width ($P = 0.03$), with nonsignificant positive relationships with (**L**) molar acellular cementum on lingual ($P = 0.09$) and buccal ($P = 0.05$) aspects. DE, dentin; PDL, periodontal ligament.

Dental Disease in HPP

The severity of human HPP is remarkably broad-ranging and spans life-threatening forms (infantile and perinatal) to milder forms (prenatal benign, childhood, adult, and odontohypophosphatasia; Whyte 2012). Skeletal defects include rickets during growth or osteomalacia in adult life, fractures, and bone pain. Dental defects commonly manifest in HPP, affecting cementum, dentin, enamel, and periodontal bone (Foster, Nociti, et al. 2014; Foster, Ramnitz, et al. 2014). We hypothesized that murine dental hard tissues are exceptionally sensitive in HPP because odontohypophosphatasia affects only the dentition, despite characteristic serum biochemical findings (Reibel et al. 2009). At present, 280 *ALPL* mutations have been identified for HPP (www.sesep.uvsq.fr), with often unclear genotype-phenotype relationships, including that for odontohypophosphatasia, where 21 *ALPL* mutations have been recorded within 8 of the 12 exons. Mild HPP can result from heterozygosity for missense mutations with a dominant-negative effect (i.e., inhibiting the enzymatic activity of the heterodimer), and these mutations sometimes localize to domains of TNAP affecting dimerization or allosteric properties (Fauvert et al. 2009).

The $Alpl^{-/-}$ mouse, featuring loss of TNAP, has been a useful model for studying the skeletal manifestations of the severe infantile form of HPP (Narisawa et al. 1997; Fedde et al. 1999). We have analyzed the dental pathologies in the $Alpl^{-/-}$ mouse, demonstrating inhibition of acellular cementum formation, delayed alveolar bone mineralization, disruption of odontoblast function and dentin mineralization, and enamel defects (McKee et al. 2011; Foster et al. 2012; Yadav et al. 2012; Foster, Nagatomo, et al. 2013; Zweifler et al. 2015). However, the severity of disease and shortened life span of these mice prevent long-term studies of the HPP skeleton and dentition, including investigations to rescue dental tissues.

A116T Mouse Model for Odontohypophosphatasia

To generate a mouse model of mildly decreased ALP and odontohypophosphatasia, we selected the *Alpl* c.346G>A point mutation, corresponding to an A116T substitution in a highly conserved residue adjacent to the enzyme active site (Silvent et al. 2014). Previous work by in vitro analysis reported a dominant-negative effect of this mutation (Lia-Baldini et al. 2001; Fauvert et al. 2009; Ishida et al. 2011), and our in vitro expression assays confirmed those findings. Plasma ALP of $Alpl^{+/A116T}$ heterozygotes ranged from 34% to 68% of the WT, with a mean reduction of 50%, consistent with the variation observed in the original HPP kindred (Hu et al. 2000). Broad-ranging ALP is likely related to instances of observed lack of penetrance in human subjects with HPP, and the same applies to mouse models. Still, the discovery of an observable dental phenotype in $Alpl^{+/A116T}$ where ALP is mildly reduced has prompted us to develop a full study on heterozygous $Alpl^{+/-}$ mice, as it is possible that carriers of HPP mutations may not be entirely asymptomatic.

Based on the presentation in this family, we predicted primarily dental manifestations in $Alpl^{+/A116T}$ mice, including defective formation of cementum, dentin, and enamel. Analysis of these $Alpl^{+/A116T}$ mice revealed no detectable defects in the skeleton except for alterations in cranial and alveolar bone and teeth. These findings validate this *Alpl* mutation as primarily affecting the murine craniofacial region. However, the $Alpl^{+/A116T}$ mouse presented a milder-than-expected dental phenotype respective to the clinical presentation in the human kindred. The $Alpl^{+/A116T}$ phenotype was primarily observed as hypomineralization of alveolar bone and cellular cementum, with minor changes in acellular cementum and no significant dentin or enamel defects, or premature loss of teeth. The importance of TNAP to cementogenesis was further supported by a significant positive correlation of incisor acellular cementum to plasma ALP and nonsignificant trends for molars. We previously identified mouse incisors as being more sensitive to disturbance in *Alpl*/TNAP, possibly due to their rapid and continuous formation, and/or an altered P_i:PP_i ratio (i.e., inorganic phosphate to inorganic pyrophosphate; Foster, Nagatomo, et al. 2013; Zweifler et al. 2015).

Two limitations of this model should be acknowledged—namely, the mildly affected periodontal structure and function and the lack of tooth loss. However, the model does provide a viable mouse with dentoalveolar effects of HPP, and several important insights were gained: (1) Teeth and periodontia developed and functioned despite a moderate reduction in ALP; (2) alterations in cementum and correlation of incisor cementum to residual plasma ALP activity supported cumulative data indicating that this tissue is highly dependent on TNAP activity; and (3) alveolar bone was identified as a target tissue in HPP, where emphasis is more often placed on cementum and dentin defects. Observed mineralization defects in alveolar bone in $Alpl^{+/A116T}$ mice may be related to the continuous rapid turnover rate of this tissue compared with other bones (Sodek and McKee 2000), prompting a higher requirement for local TNAP function. The cause for the apparent increase in resorption of alveolar and interproximal bone in $Alpl^{+/A116T}$ mice is not clear, although it may be related to altered tissue properties, constant mechanical loads from chewing, and/or subtle changes in periodontal attachment or function. The fact that resorptive lesions were observed only with advanced age supports the hypothesis that this is a functional response that gradually arises after teeth enter occlusion.

Overall, the $Alpl^{+/A116T}$ mouse model provides valuable insights into the effects of a relatively mild reduction of TNAP activity on the dentoalveolar complex, highlighting changes in alveolar bone and providing a new model for testing potential therapies.

References

Aspden RM. 2003. Mechanical testing of bone ex vivo. Methods Mol Med. 80:369–379.

Bouxsein ML, Boyd SK, Christiansen BA, Guldberg RE, Jepsen KJ, Muller R. 2010. Guidelines for assessment of bone microstructure in rodents using micro–computed tomography. J Bone Miner Res. 25:1468–1486.

Fauvert D, Brun-Heath I, Lia-Baldini AS, Bellazi L, Taillandier A, Serre JL, de Mazancourt P, Mornet E. 2009. Mild forms of hypophosphatasia mostly result from dominant negative effect of severe alleles or from compound heterozygosity for severe and moderate alleles. BMC Med Genet. 10:51.

Fedde KN, Blair L, Silverstein J, Coburn SP, Ryan LM, Weinstein RS, Waymire K, Narisawa S, Millán JL, MacGregor GR, et al. 1999. Alkaline phosphatase knock-out mice recapitulate the metabolic and skeletal defects of infantile hypophosphatasia. J Bone Miner Res. 14:2015–2026.

Foster BL. 2012. Methods for studying tooth root cementum by light microscopy. Int J Oral Sci. 4:119–128.

Foster BL, Nagatomo KJ, Nociti FH Jr, Fong H, Dunn D, Tran AB, Wang W, Narisawa S, Millán JL, Somerman MJ. 2012. Central role of pyrophosphate in acellular cementum formation. PLoS One. 7(6):e38393.

Foster BL, Nagatomo KJ, Tso HW, Tran AB, Nociti FH Jr, Narisawa S, Yadav MC, McKee MD, Millán JI, Somerman MJ. 2013. Tooth root dentin mineralization defects in a mouse model of hypophosphatasia. J Bone Miner Res. 28:271–282.

Foster BL, Nociti FH Jr, Somerman MJ. 2014. The rachitic tooth. Endocr Rev. 35:1–34.

Foster BL, Ramnitz MS, Gafni RI, Burke AB, Boyce AM, Lee JS, Wright JT, Akintoye SO, Somerman MJ, Collins MT. 2014. Rare Bone Diseases and Their Dental, Oral, and Craniofacial Manifestations. J Dent Res. 93(7):7S–19S.

Foster BL, Soenjaya Y, Nociti FH Jr, Holm E, Zerfas PM, Wimer HF, Holdsworth DW, Aubin JE, Hunter GK, Goldberg HA, et al. 2013. Deficiency in acellular cementum and periodontal attachment in bsp null mice. J Dent Res. 92:166–172.

Harmey D, Hessle L, Narisawa S, Johnson K, Terkeltaub R, Millán J. 2004. Concerted regulation of inorganic pyrophosphate and osteopontin by akp2, enpp1, and ank: an integrated model of the pathogenesis of mineralization disorders. Am J Pathol. 164:1199–1209.

Harmey D, Johnson KA, Zelken J, Camacho NP, Hoylaerts MF, Noda M, Terkeltaub R, Millán JL. 2006. Elevated skeletal osteopontin levels contribute to the hypophosphatasia phenotype in Akp2(-/-) mice. J Bone Miner Res. 21:1377–1386.

Hu JC, Plaetke R, Mornet E, Zhang C, Sun X, Thomas HF, Simmer JP. 2000. Characterization of a family with dominant hypophosphatasia. Eur J Oral Sci. 108:189–194.

Ishida Y, Komaru K, Oda K. 2011. Molecular characterization of tissue-nonspecific alkaline phosphatase with an Ala to Thr substitution at position 116 associated with dominantly inherited hypophosphatasia. Biochim Biophys Acta. 1812:326–332.

Lia-Baldini AS, Muller F, Taillandier A, Gibrat JF, Mouchard M, Robin B, Simon-Bouy B, Serre JL, Aylsworth AS, Bieth E, et al. 2001. A molecular approach to dominance in hypophosphatasia. Hum Genet. 109:99–108.

Liu J, Nam HK, Wang E, Hatch NE. 2013. Further analysis of the Crouzon mouse: effects of the FGFR2(C342Y) mutation are cranial bone-dependent. Calcif Tissue Int. 92:451–466.

McKee MD, Nakano Y, Masica DL, Gray JJ, Lemire I, Heft R, Whyte MP, Crine P, Millán JL. 2011. Enzyme replacement therapy prevents dental defects in a model of hypophosphatasia. J Dent Res. 90:470–476.

Meganck JA, Kozloff KM, Thornton MM, Broski SM, Goldstein SA. 2009. Beam hardening artifacts in micro–computed tomography scanning can be reduced by X-ray beam filtration and the resulting images can be used to accurately measure BMD. Bone. 45:1104–1116.

Millán JL. 2013. The role of phosphatases in the initiation of skeletal mineralization. Calcif Tissue Int. 93:299–306.

Millán JL, Narisawa S, Lemire I, Loisel TP, Boileau G, Leonard P, Gramatikova S, Terkeltaub R, Camacho NP, McKee MD, et al. 2008. Enzyme replacement therapy for murine hypophosphatasia. J Bone Miner Res. 23:777–787.

Narisawa S, Fröhlander N, Millán J. 1997. Inactivation of two mouse alkaline phosphatase genes and establishment of a model of infantile hypophosphatasia. Dev Dyn. 208:432–446.

Reibel A, Manière MC, Clauss F, Droz D, Alembik Y, Mornet E, Bloch-Zupan A. 2009. Orodental phenotype and genotype findings in all subtypes of hypophosphatasia. Orphanet J Rare Dis. 4:6.

Silvent J, Gasse B, Mornet E, Sire JY. 2014. Molecular evolution of the tissue-nonspecific alkaline phosphatase allows prediction and validation of missense mutations responsible for hypophosphatasia. J Biol Chem. 289:24168–24179.

Sodek J, McKee MD. 2000. Molecular and cellular biology of alveolar bone. Periodontol. 24:99–126.

Umoh JU, Sampaio AV, Welch I, Pitelka V, Goldberg HA, Underhill TM, Holdsworth DW. 2009. In vivo micro-CT analysis of bone remodeling in a rat calvarial defect model. Phys Med Biol. 54:2147–2161.

Whyte MP. 2012. Hypophosphatasia. In: Thakker RV, Whyte MP, Eisman J, Igarashi T, editors. Genetics of bone biology and skeletal disease. San Diego (CA): Elsevier. p. 337–360.

Yadav MC, de Oliveira RC, Foster BL, Fong H, Cory E, Narisawa S, Sah RL, Somerman M, Whyte MP, Millán JL. 2012. Enzyme replacement prevents enamel defects in hypophosphatasia mice. J Bone Miner Res. 27(8):1722–1734.

Zweifler LE, Patel MK, Nociti FH, Wimer HF, Millan JI, Somerman MJ, Foster BL. 2015. Counter-regulatory phosphatases TNAP and NPP1 temporally regulate tooth root cementogenesis. Int J Oral Sci. 23;7(1):27–41.

Periodontal Defects in the A116T Knock-in Murine Model of Odontohypophosphatasia

B.L. Foster[1]*, C.R. Sheen[2]*, N.E. Hatch[3], J. Liu[3], E. Cory[4], S. Narisawa[2], T. Kiffer-Moreira[2], R.L. Sah[4], M.P. Whyte[5,6], M.J. Somerman[1], and J.L. Millán[2]

Appendix

Methods

Mutation Selection and Expression Analysis

The *Alpl* c.346G>A mutation, corresponding to an A116T substitution, was selected for knock-in based on its established adult-onset and predominantly dental phenotype in humans (Hu et al. 2000) and dominant-negative effect in vitro (Lia-Baldini et al. 2001; Fauvert et al. 2009; Ishida et al. 2011). Cotransfection studies were performed to evaluate the effect of A116T heterozygosity on the mouse tissue nonspecific alkaline phosphatase enzyme. A pcDNA3.1 expression vector containing the mouse tissue nonspecific alkaline phosphatase cDNA sequence with a C-terminal FLAG tag was mutated using a Quickchange Site Directed Mutagenesis kit (Stratagene, San Diego, CA, USA) and primers mA116Tf/mA116Tr (Appendix Table 1) according to the manufacturer's directions to introduce the A116T mutation. Equimolar amounts of wild-type and A116T mutant plasmid were cotransfected by electroporation into COS1 cells, as described previously (Otero et al. 2012). Media containing secreted proteins was collected 60 h after electroporation and used for enzyme analysis. All kinetic measurements were performed in triplicate at 25 °C. To normalize the amount of protein, microtiter plates were coated with 0.1 µg/mL of M2 antibody (Sigma-Aldrich, St. Louis, MO, USA). The relative catalytic activities of bound enzymes were measured at 405 nm as a function of time using *p*-nitrophenylphosphate (20 mM) as a substrate at pH 9.8 in 1M diethanolamine buffer containing 1mM $MgCl_2$ and 20µM $ZnCl_2$.

Knock-in Vector Selection, Design, and Synthesis

Generation of the knock-in mouse line and all experiments involving mice were approved by the Institutional Animal Care and Use Committee of the Sanford Burnham Medical Research Institute (La Jolla, CA, USA). The *Alpl* c.346G>A mutation, corresponding to an A116T substitution, was selected for knock-in based on its predominantly dental phenotype in humans (Hu et al. 2000) and dominant-negative effect in vitro (Lia-Baldini et al. 2001; Fauvert et al. 2009; Ishida et al. 2011). Polymerase chain reaction (PCR) primers (all primer sequences used are listed in Appendix Table 1) were designed to amplify a region of *Alpl* spanning 7,225 base pairs from intron 4 to intron 8 (nucleotides 137,747,632 to 137,754,856 of chromosome 4 in GCRm38/mm10 mouse genome assembly), including the site of the A116T mutation in exon 5. Reactions contained 1× KAPA HiFi Buffer (KAPA Biosystems, Woburn, MA, USA), 0.3mM dNTPs, 0.3µM each 5′-phosphorylated primer (Alpl fragment F/R), 50 ng of C57BL6 mouse genomic DNA, and 0.5 U of KAPA HiFi DNA Polymerase (KAPA Biosystems). Thermal cycling parameters were 95 °C for 5 min, 30 cycles of 98 °C for 20 s, 62 °C for 15 s, 72 °C for 5 min, and a final step of 72 °C for 5 min. PCR products were run on an agarose gel, and bands of appropriate size were purified using a QIAquick Gel Extraction kit (Qiagen, Hilden, Germany). The purified fragment was then blunt-end cloned into pSMART-LCkan (Lucigen, Middleton, WI, USA) according to the manufacturer's instructions. The resulting plasmid was named pSMART-LCkan-Alpl.

A PCR fragment containing the murine phosphoglycerate kinase promoter, a neomycin resistance gene, and the bovine growth hormone polyadenylation sequence was amplified from plasmid PGKneobpA. Reactions contained 1× Platinum *Taq* High Fidelity buffer (Invitrogen, Carlsbad, CA, USA), 2mM $MgSO_4$, 0.2mM dNTPs, 0.2µM primers (BamHI-loxP-neoF/BamHI-loxP-neoR), 10 ng of PGKneobpA template, and

[1]National Institute of Arthritis and Musculoskeletal and Skin Diseases, National Institutes of Health, Bethesda, MD, USA
[2]Sanford Children's Health Research Center, Sanford-Burnham Medical Research Institute, La Jolla, CA, USA
[3]Department of Orthodontics and Pediatric Dentistry, School of Dentistry, University of Michigan, Ann Arbor, MI, USA
[4]Department of Bioengineering, University of California, San Diego, La Jolla, CA, USA
[5]Center for Metabolic Bone Disease and Molecular Research, Shriners Hospital for Children, St. Louis, MO, USA
[6]Division of Bone and Mineral Diseases, Washington University School of Medicine, St. Louis, MO, USA
*Authors contributing equally to this article.

Corresponding Author:
J.L. Millán, Sanford Children's Health Research Center, Sanford-Burnham Medical Research Institute, La Jolla, CA, USA.
Email: millan@sanfordburnham.org

Appendix Figure. Mineralization defects in dentoalveolar tissues in *Alpl*^{-/-} mice. Images from *Alpl*^{-/-} mandibles at 24 d postnatal show dentoalveolar defects in resulting from absence of tissue nonspecific alkaline phosphatase. Compared with (**A**) wild-type (WT) mandibles, (**B**) *Alpl*^{-/-} mandibles are smaller and, by radiography, feature reduced size and mineralization of bone and teeth, as well as delays in molar (M1 to M3) and incisor (INC) development. By micro–computed tomography, well-mineralized bone and tooth structures of (**C–E**) the WT mandible are observed to be severely hypomineralized (and below threshold; arrow for bone, asterisk for dentin) in (**F–H**) *Alpl*^{-/-} mandibles, including alveolar and mandibular bone, and tooth root dentin. By histology, dentoalveolar structures of (**I, J, M**) WT molars—including alveolar bone (AB), acellular cementum (AC; arrow), periodontal ligament (PDL), dentin (DE), and cellular cementum (CC)—are organized and functional, while (**K, L, O**) *Alpl*^{-/-} mouse molars exhibit osteomalacia of the surrounding alveolar bone (asterisk); acellular cementum is absent; PDL is detached and disorganized; and dentin and cellular cementum are hypomineralized. Yellow boxes in I and K represent regions shown in J and L, respectively. Red boxes in I and K represent regions shown in M and O, respectively. (**N, P**) *Alpl*^{-/-} mouse incisors are severely affected in parallel to molars, with hyoplastic and hypomineralized root analogue (lingual) dentin, lack of AC (arrow), and PDL disorganization.

1 U of Platinum Taq High Fidelity Polymerase (Invitrogen). Thermal cycling parameters were 94 °C for 2 min, 30 cycles of 94 °C for 15 s, 60 °C for 30 s, 68 °C for 2 min, and a final step of 68 °C for 5 min. The resulting plasmid was gel purified as described above, cloned into pCR2.1-TOPO (Invitrogen) according to the manufacturer's instructions, and named pCR2.1-BamHIloxPneo.

Plasmid pSMART-LCkan-Alpl was digested with *Bam*HI and treated with Antarctic phosphatase (New England Biolabs, Ipswich, MA, USA) to prevent self-ligation. Plasmid pCR2.1-BamHIloxPneo was digested with *Bam*HI, and the fragment corresponding to the neomycin cassette was gel-purified as described, then ligated into pSMART-LCkan-Alpl using T4 DNA ligase (New England Biolabs) to produce plasmid

Appendix Table 1. Oligonucleotide Primers Used in This Study.

Primer Name	Primer Sequence (5′-3′)	Product Size
BamHI-loxP-neoF	GGATCCATAACTTCGTATAGCATACATTAT**ACGAAGTTAT**GTAGGGGAGGCGCTTTTCCCAAG	1648 bp
BamHI-loxP-neoR	*GGATCC***ATAACTTCGTATAATGTATGCTAT ACGAAGTTAT**AAGCCATAGAGCCCACCGCATCC	
Alpl fragment F	CCCAAGAAAGAGTGCACACA	7225 bp
Alpl fragment R	GGGGCTCATCTGCTGCACAGCTTAA	
A116T locus F	CCTTGAGTTCTGCCAGGGTA	354 bp
A116T locus R	CTTCGATGGCTCACCAGCAT	
CreF	GCGGTCTGGCAGTAAAAACTATC	102 bp
CreR	GTGAAACAGCATTGCTGTCACTT	
mA116Tf	CGGGCACTGCCACT<u>A</u>CCTACTTGTGTGGC	
mA116Tr	GCCACACAAGTAGG<u>T</u>AGTGGCAGTGCCCG	

*Bam*HI cleavage site is italicized, loxP site is shown in bold, and the nucleotide mutated in A116T is underlined.

Appendix Table 2. Plasma Biochemical Analysis.

Parameter	WT	$Alpl^{+/A116T}$
Calcium, mmol/L	2.28 ± 0.08	2.29 ± 0.08
Phosphorus, mmol/L	2.34 ± 0.29	2.35 ± 0.34
Alkaline phosphatase activity, U/L	50 ± 10.2	25.6 ± 5.4[a]

Plasma was collected from wild-type (WT; $n = 7$) and $Alpl^{+/A116T}$ ($n = 9$) mice at 120 d postnatal for analysis.
[a] $P < 0.001$. Two-tailed Student's *t* test.

Appendix Table 3. Relative Alkaline Phosphatase Activity of WT, Mutant, and WT/Mutant Mouse Tissue Nonspecific Alkaline Phosphatases Expressed In Vitro.

Enzyme	Relative Activity, %
116A (WT) construct	100.0 ± 2.3
116A/T cotransfection	32.5 ± 2.2
116T (mutant) construct	Not detected

Relative activity is defined as paranitrophenyl phosphatase activity relative to the wild-type (WT) enzyme. Values are means ± SD of triplicate measurements.

Appendix Table 4. Micro–computed Tomography Analysis of Femora.

Parameter	WT	$Alpl^{+/A116T}$
Tt.Ar, mm^2	1.44 ± 0.26	1.37 ± 0.14
Ct.Ar, mm^2	0.85 ± 0.10	0.83 ± 0.06
Ct.Ar/Tt.Ar, %	59.4 ± 4.40	60.4 ± 3.00
Ct.Th, mm	0.16 ± 0.01	0.15 ± 0.00
TMD, g/cm^3	1.07 ± 0.04	1.06 ± 0.04
TV, mm^3	4.01 ± 0.11	4.27 ± 0.15
BV, mm^3	0.46 ± 0.04	0.49 ± 0.04
BV/TV, %	11.3 ± 1.00	11.3 ± 0.60
Tb.Th, mm	0.046 ± 0.002	0.045 ± 0.001
Tb.Sp, mm	0.22 ± 0.01	0.21 ± 0.00
Tb.N, 1/mm	2.45 ± 0.16	2.52 ± 0.11
SMI	1.69 ± 0.11	1.72 ± 0.07
BMD, g/cm^3	0.22 ± 0.02	0.22 ± 0.01

Cortical and trabecular bone parameters of wild-type (WT; $n = 7$) and $Alpl^{+/A116T}$ ($n = 9$) mice femora were analyzed at 120 d postnatal. No significant differences noted ($P > 0.05$).
BV, bone volume; BMD, bone mineral density; Ct.Ar, cortical bone area; Ct.Th, cortical thickness; Ct.Ar/Tt.Ar, cortical area fraction; SMI, structure model index; Tb.N, trabecular number; Tb.Th, trabecular thickness; Tb.Sp, trabecular spacing; TMD, tissue mineral density; Tt.Ar, total cross-sectional tissue area; TV, tissue volume.

pSMART-LCkan-Alpl-loxPneo. Site-directed mutagenesis to introduce the A116T point mutation was performed using a Quickchange Site Directed Mutagenesis kit (Stratagene, San Diego, CA, USA) with mutagenic primers mA116Tf and mA116Tr, according to the manufacturer's instructions. All plasmids were sequenced after construction by Genewiz (La Jolla, CA, USA).

The final targeting construct (Fig. 1A) was composed of long and short homology arms (5,696 and 1,529 base pairs, respectively), separated by a neomycin resistance cassette flanked by direct loxP repeats.

The vector containing the targeting construct was linearized by digestion with *Xho*I and purified by ethanol precipitation, then electroporated into Bruce4 C57BL/6 embryonic stem (ES) cells as described (Nagy et al. 2003). Neomycin-resistant colonies were expanded for DNA extraction. Successful homologous recombination and integration of the targeting

Appendix Table 5. Mechanical Properties of Femora as Determined by 3-point Bending.

Parameter	WT	$Alpl^{+/A116T}$
Maximum stiffness, N/mm	14.0 ± 0.2	12.8 ± 0.8
Failure load, N	16.9 ± 0.5	17.0 ± 0.4
Fracture load, N	11.4 ± 1.5	12.2 ± 1.3
Work to fracture	0.96 ± 0.12	0.92 ± 0.16

Femora of wild-type (WT; $n = 6$) and $Alpl^{+/A116T}$ ($n = 4$) mice were analyzed at 120 d postnatal. No significant differences noted ($P > 0.05$).

construct into the ES cell genome was confirmed using the Southern hybridization method described previously (Narisawa et al. 1997). The locus surrounding the point mutation was amplified using primers A116T-locus-F/A116T-locus-R, and the product was sequenced to confirm introduction of the mutation into the ES cell genome (Genewiz, San Diego, CA,

Appendix Table 6. Micro–computed Tomography Analysis of Cranial Bones.

	Frontal Bone		Parietal Bone	
Parameter	WT	$Alpl^{+/A116T}$	WT	$Alpl^{+/A116T}$
BMC, mg	0.108 ± 0.015	0.100 ± 0.012	0.132 ± 0.019	0.119 ± 0.020
BMD, mg/cm^3	625 ± 48	627 ± 32	738 ± 23	724 ± 23
TMC, mg	0.088 ± 0.011	0.082 ± 0.008	0.114 ± 0.015	0.107 ± 0.18
TMD, mg/cm^3	746 ± 21	746 ± 24	776 ± 19	773 ± 26
TV, mm^3	0.684 ± 0.072	0.691 ± 0.043	0.883 ± 0.046	0.847 ± 0.029
BV, mm^3	0.683 ± 0.073	0.693 ± 0.044	0.885 ± .0045	0.850 ± 0.031
BS/BV, mm^2/mm^3	29.23 ± 2.67	30.10 ± 1.10	15.59 ± 1.16	18.02 ± 3.17[a]
Tb.Th, mm	0.069 ± 0.006	0.067 ± 0.002	0.129 ± 0.010	0.114 ± 0.019[a]
Tb.N, 1/mm	9.92 ± 0.83	10.41 ± 0.63	6.88 ± 0.40	7.62 ± 1.12[a]
Tb.Sp, mm	0.033 ± 0.010	0.030 ± 0.006	0.017 ± 0.007	0.020 ± 0.003

Frontal and parietal bones were compared for wild-type (WT; $n = 7$) and $Alpl^{+/A116T}$ ($n = 9$) mice at 120 d postnatal.
BS, bone surface; BV, bone volume; BMC, bone mineral content; BMD, bone mineral density; SMI, structure model index; Tb.N, trabecular number; Tb.Th, trabecular thickness; Tb.Sp, trabecular spacing; TMC, tissue mineral content; TMD, tissue mineral density; TV, tissue volume.
[a]$P < 0.05$. Two-tailed Student's t test.

Appendix Table 7. Micro–computed Tomography Analysis of Dental Tissues.

	TV, mm^3	BV, mm^3	BV/TV, %[a]	TMD, g HA/cm^3	Thickness, μm
Crown enamel					
WT	0.51 ± 0.02	0.18 ± 0.01	35.83 ± 0.57	1.75 ± 0.02	62.1 ± 0.7
$Alpl^{+/A116T}$	0.50 ± 0.02	0.19 ± 0.01	36.69 ± 0.89[b]	1.75 ± 0.04	62.7 ± 0.9
Crown dentin					
WT	0.51 ± 0.02	0.47 ± 0.02	92.00 ± 0.61	ND	ND
$Alpl^{+/A116T}$	0.50 ± 0.02	0.46 ± 0.02	91.55 ± 0.58	ND	ND
Root dentin					
WT	0.72 ± 0.04	0.64 ± 0.03	89.26 ± 0.20	1.07 ± 0.01	153.9 ± 4.5
$Alpl^{+/A116T}$	0.71 ± 0.05	0.63 ± 0.05	88.22 ± 0.75[c]	1.07 ± 0.01	151.0 ± 6.1

First mandibular molars were compared at 120 d postnatal in wild-type (WT; $n = 7$) and $Alpl^{+/A116T}$ mice ($n = 9$). Values are reported as means ± SD.
BV, bone volume; ND, not determined; TMD, tissue mineral density; TV, tissue volume.
[a]For analysis of enamel, TV was measured for the total crown volume, and BV was measured for enamel layer; therefore, BV/TV is the percentage volume of enamel in the crown (BV_{enamel}/TV_{crown}). For analysis of dentin, TV and BV refer solely to the dentin layer proper.
[b]$P < 0.05$. Independent-samples t test.
[c]$P < 0.01$. Independent-samples t test.

USA). ES cells were injected into blastocysts of B6(Cg)-Tyr^{c-2J}/J albino mice (stock 000058; The Jackson Laboratory, Bar Harbor, ME, USA), then transferred into pseudopregnant recipient C57BL6 mothers.

Chimeric offspring male mice were bred with C57BL6 female mice, and DNA was extracted for PCR from the tail clippings of offspring. Reactions contained 1× Platinum *Taq* buffer, 1.5mM MgCl$_2$, 0.2mM dNTPs, 0.2μM primers (A116TlocusF/A116TlocusR), 100 ng of genomic DNA template, and 1 U of Platinum *Taq* DNA Polymerase (Invitrogen). Thermal cycling parameters were 94 °C for 2 min, 30 cycles of 94 °C for 15 s, 60 °C for 30 s, 72 °C for 30 s, and a final step of 72 °C for 5 min. PCR products were sequenced by Genewiz to confirm transmission of the point mutation (Fig. 1B). Female mice carrying the A116T mutation were then bred with male B6.129S4-$Meox2^{CreSor}$ ubiquitous Cre expression mice (stock 003755; The Jackson Laboratory; Tallquist and Soriano 2000) to excise the neomycin cassette. Offspring carrying the A116T mutation were then bred until no transgene was detected by PCR using Platinum *Taq* Polymerase, as described above, with primers CreF/CreR. The $Alpl^{A116T}$ mouse line was maintained by breeding wild-type mice with A116T heterozygotes ($Alpl^{+/A116T}$), and all offspring were genotyped by DNA sequencing as described above.

Micro–computed Tomography

Femurs were cleaned of soft tissue and fixed in 4% paraformaldehyde. Samples were imaged on a Skyscan 1076 micro–computed tomography (micro-CT) scanner (Kontich, Belgium) with parameters of 9-μm voxel size, 50 kVp, 200 μA, using a 0.5-mm aluminum filter. Mineral density was determined by calibration of images against 2-mm-diameter hydroxyapatite rods (0.25 and 0.75 gHA/cm^3). A beam-hardening correction algorithm was applied prior to image reconstruction. Sample data were visualized and quantified using Dataviewer and CTAn software (Skyscan, Kontich, Belgium). Regions of interest were determined using established guidelines for skeletally mature mice (Bouxsein et al. 2010). Cortical bone analysis was performed on the femoral midshaft, using a region of

interest that was offset 3.6 mm proximally from the distal growth plate and extended 900 μm. The cortical bone in this region was selected by contouring the periosteal tissue and excluding the marrow cavity. A global threshold was used to identify cortical bone, and an erosion of 1 pixel was performed to eliminate partial volume effects. This region of cortical bone was used to determine cross-sectional tissue area, cross-sectional cortical bone area (Ct.Ar), cortical bone area fraction (Ct.Ar/ cross-sectional tissue area), cross-sectional bone thickness, and tissue mineral density (TMD).

Trabecular bone analysis was performed at the distal femoral metaphysis. The region of interest was selected 360 μm proximally to the distal growth plate and extended proximally 1.8 mm. The trabecular region was selected by contouring. An adaptive threshold (using the mean maximum and minimum pixel intensity values of the surrounding ten pixels) was used to identify trabecular bone, and an erosion of 1 pixel was performed to eliminate partial volume effects. This region of trabecular bone was used to determine tissue volume (TV), bone volume (BV), bone volume fraction (BV/TV), trabecular thickness (Tb.Th), trabecular separation (Tb.Sp), trabecular number (Tb.N), structure model index, and bone mineral density.

For craniofacial bone analysis, dissected skulls were fixed, then scanned on the eXplore Locus SP micro-CT imaging system (GE Healthcare Pre-clinical Imaging, London, ON, Canada) with parameters of 18-μm isotropic voxel resolution, 80 kV, 80 mA, with an exposure time of 1,600 ms using the Parker method scan technique, which rotates the sample 180°, plus a fan angle of 20°. Scans were calibrated to a hydroxyapatite phantom, and 3-dimensional images were reconstructed at an effective voxel size of 18 μm^3. A fixed threshold of 1,400 Hounsfield units was used to discriminate mineralized tissue. Regions of interest for parietal and frontal bones were established as 1 mm in length, 1 mm in width, and a depth equivalent to thickness of bone and position starting at a 0.75-mm distance from sagittal and coronal sutures, as described previously (Liu et al. 2013). Parameters of bone volume, density, and structure were measured using MicroView software (version 2.2, GE Healthcare Pre-clinical Imaging) and established algorithms (Meganck et al. 2009; Umoh et al. 2009). Parameters analyzed included bone mineral content (BMC), bone mineral density, tissue mineral content, TMD, TV, BV, BV/TV, bone surface (BS), BS/BV, Tb.Th, Tb.N, and Tb.Sp. Student's *t* tests comparing quantitative results were performed to establish statistically significant differences between genotypes. Micro-CT bone data were analyzed and are reported in accordance with recommendations (Bouxsein et al. 2010).

For dentoalveolar analysis, dissected mandibles were scanned on a Scanco Medical μCT 35 (Scanco Medical AG, Brüttisellen, Switzerland) with parameters of 6-μm voxel size, 55 KVp, 145 mA, with a 0.36° rotation step (180° angular range) and a 400-ms exposure per view. Scanco μCT software (HP, DECwindows Motif 1.6) was used for 3D reconstruction and image viewing. Mandible z-stacks were exported as DICOM files and reoriented using ImageJ software (1.48r), with comparable coronal, sagittal, and transverse planes of section chosen for comparison. Enamel, crown (enamel and dentin), and root dentin were analyzed using parameters of TV, BV, BV/TV, and TMD. Alveolar bone in the furcation region of the first mandibular molar roots was additionally analyzed by Tb.N, Tb.Th, Tb.Sp, and BS/BV. Alveolar bone on the lingual aspect of the first molar was analyzed by TV, BV, BV/TV, and TMD.

Appendix References

Bouxsein ML, Boyd SK, Christiansen BA, Guldberg RE, Jepsen KJ, Muller R. 2010. Guidelines for assessment of bone microstructure in rodents using micro–computed tomography. J Bone Miner Res. 25:1468–1486.

Fauvert D, Brun-Heath I, Lia-Baldini AS, Bellazi L, Taillandier A, Serre JL, de Mazancourt P, Mornet E. 2009. Mild forms of hypophosphatasia mostly result from dominant negative effect of severe alleles or from compound heterozygosity for severe and moderate alleles. BMC Med Genet. 10:51.

Hu JC, Plaetke R, Mornet E, Zhang C, Sun X, Thomas HF, Simmer JP. 2000. Characterization of a family with dominant hypophosphatasia. Eur J Oral Sci. 108:189–194.

Ishida Y, Komaru K, Oda K. 2011. Molecular characterization of tissue-non-specific alkaline phosphatase with an Ala to Thr substitution at position 116 associated with dominantly inherited hypophosphatasia. Biochim Biophys Acta. 1812:326–332.

Lia-Baldini AS, Muller F, Taillandier A, Gibrat JF, Mouchard M, Robin B, Simon-Bouy B, Serre JL, Aylsworth AS, Bieth E, et al. 2001. A molecular approach to dominance in hypophosphatasia. Hum Genet. 109:99–108.

Liu J, Nam HK, Wang E, Hatch NE. 2013. Further analysis of the Crouzon mouse: effects of the FGFR2(C342Y) mutation are cranial bone-dependent. Calcif Tissue Int. 92:451–466.

Nagy A, Gertsenstein M, Vintersten K, Behringer R. 2003. Manipulating the mouse embryo: a laboratory manual. New York (NY): Cold Spring Harbor Laboratory Press.

Narisawa S, Fröhlander N, Millán J. 1997. Inactivation of two mouse alkaline phosphatase genes and establishment of a model of infantile hypophosphatasia. Dev Dyn. 208:432–446.

Otero JE, Gottesman GS, McAlister WH, Mumm S, Madson KL, Kiffer-Moreira T, Sheen C, Millán JL, Ericson KL, Whyte MP. 2012. Severe skeletal toxicity from protracted etidronate therapy for generalized arterial calcification of infancy. J Bone Miner Res. 28:419–430.

Tallquist MD, Soriano P. 2000. Epiblast-restricted Cre expression in MORE mice: a tool to distinguish embryonic vs. extra-embryonic gene function. Genesis. 26:113–115.